Measurement of Cryogenic Target Position and Implosion Core Offsets on OMEGA

Introduction

Direct-drive inertial confinement fusion experiments are performed by uniformly illuminating spherical cryogenic deuterium–tritium (DT) fuel-bearing CH shell capsules with high-power laser beams.[1] A goal of inertial confinement fusion (ICF) experiments is thermonuclear ignition and gain; in order for this to occur, the fuel must be symmetrically compressed to high areal densities, i.e., at least 0.3 g/cm^2, and the central hot-spot temperature must be at least 10 keV (Refs. 2–4). Target performance is degraded by imperfections in symmetric laser illumination and in the target itself. Perturbations of the intensity in the low Legendre modes ($\ell \le 6$), which may include target offset, can distort the core at stagnation while higher-mode ($\ell \ge 6$) perturbations lead to Rayleigh–Taylor unstable growth, target breakup, and mixing of the materials in the shell and fuel.[5] These perturbations reduce the peak temperature and areal density of the final fuel region; therefore, minimizing them is desired. Assessing the performance of the implosions requires one to simulate the implosion with one-dimensional (Ref. 6) and multidimensional hydrocode simulations,[7] and the multidimensional simulations require accurate values of target offset from beam aiming to accurately simulate the implosions. This article describes our method of measuring initial target offset from the aim point of the beams and determining the core offset resulting from target offset from this aim point.

Measurements of Initial Target Offsets

Targets illuminated by the 60 beams of OMEGA at intensities ranging from ~10^{14} to ~10^{15} W/cm^2 emit x rays, easily imaged by pinhole cameras, in the range of 1 to 10 keV. A set of x-ray pinhole cameras (XRPC's) is used on OMEGA to precisely align the laser beams to the target center.[8] This is currently done to an accuracy of ~7-μm rms (root mean square) using a set of fixed and retractable XRPC's, all digitally recording the images with charge-injection–device (CID) cameras.[9] This set includes five fixed XRPC's, which are attached to the OMEGA target chamber, and six ten-inch-manipulator (TIM)–based XRPC's, which are retractable through a vacuum gate valve. The fixed XRPC's remain in use during both cryogenic target and non-cryogenic target implosions.

Since the targets used to precisely align the OMEGA beams by locating the x-ray spot emitted by each beam on pointing shots[8] are positioned by visible light cameras, all other non-cryogenic targets are aligned to this same point. This position is referred to as target chamber center (TCC), although it is really the aim point of the beams determined through precision pointing using the CID-based XRPC's. The precise locations of TCC in the XRPC images are determined by measuring x rays emitted by a precisely located non-cryogenic target; these TCC reference images are all from target shots taken on the same day as the cryogenic target shots. This effectively eliminates the possibility of changes in the XRPC's contributing to the determined offsets. Positioning cryogenic targets is complicated by the need to view the cryogenic target through windows in the shroud that maintains the target at near the triple point (~20 K). These windows refract the light passing through them by an amount that must be determined by testing prior to the actual shots. Furthermore, vibration of the cryogenic target stalk while the shroud is in place and impulses transmitted to this stalk when the shroud is retracted (~50 ms before the shot) can misplace the cryogenic target. This can cause the cryogenic target to be offset from TCC at t_0 (the beginning of the laser pulse).

The example of a non-cryogenic target XRPC image in Fig. 151.25(a) shows a 1.5 × 1.5-mm region at the target plane. The outer edge of the x-ray emission, which occurs at t_0, is determined from the maximum gradient using a Sobel filter.[10] This set of positions is then fit to a circle whose center position is then determined [overlaid circle and central cross in Fig. 151.25(a)]. An example cryogenic target x-ray image is shown in Fig. 151.25(b). The fusion neutrons created by the implosion of this target ($y_n = 3 \times 10^{13}$) have generated copious amounts of noise including a gamma-ray–induced background, single-pixel upsets caused by neutron-scattering events that produce protons, and line and column noise caused by similar interactions with the readout structure of the CID camera. This noise can in large part be removed by first filtering the image using a single-pixel upset detection and replacement algorithm,[11] next by removing the average line and column noise measured away from the image itself, and lastly by using a

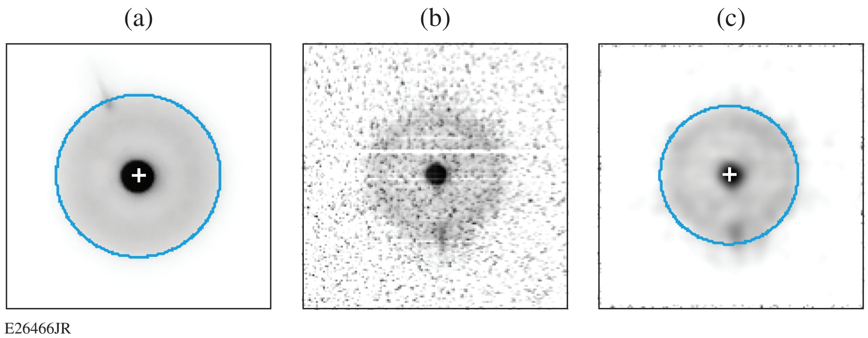

Figure 151.25
X-ray images from the OMEGA H4 x-ray pinhole camera (XRPC) charge-injection device (CID). (a) Target chamber center (TCC) reference image on shot 85780, (b) unfiltered image from a cryogenic target on shot 85784, and (c) filter image of the same. Both the reference image (a) and the filtered cryogenic target shot image (c) have the best-fit positions indicated by a circle and a cross in the center.

median filter to reduce additional noise. The result of performing this noise removal procedure is shown in Fig. 151.25(c), and the position of the center of the cryogenic target is determined in like fashion to the reference non-cryogenic target. The pixel-location differences of the two centers are then converted to microns, and the difference between the cryogenic target position and the reference target position is a measured projected offset at t_0.

Two methods are employed to determine the three-space offset $\mathbf{r}$ of cryogenic targets at t_0 from TCC. Both methods use the projected offsets of the cryogenic target centers at t_0 from the reference non-cryogenic targets whose centers are at TCC. The view vectors for each XRPC are related to the target chamber vector coordinates by the following formulas:

$$\mathbf{q}=\frac{\mathbf{z}\times\mathbf{v}}{\left|\mathbf{z}\times\mathbf{v}\right|}, \tag{1}$$

$$\mathbf{p}=\frac{\mathbf{v}\times\mathbf{q}}{\left|\mathbf{v}\times\mathbf{q}\right|}, \tag{2}$$

where $\mathbf{q}$ is the horizontal vector in an image whose view direction is $\mathbf{v}$ and the normalized cross product of $\mathbf{z}$ (straight up) and $\mathbf{v}$, while the vertical direction in the image plane $\mathbf{p}$ is given by the normalized cross product of $\mathbf{v}$ and $\mathbf{q}$ (see Fig. 151.26).

The XRPC's provide multiple quasi-orthogonal views of the target x-ray emission, from which $\mathbf{r}$ can be determined. The first method uses the projected offsets from pairs of cameras to determine the three-space offsets. For an offset in space of $\mathbf{r}$, the projections of $\mathbf{r}$ in a pair of camera views are given by

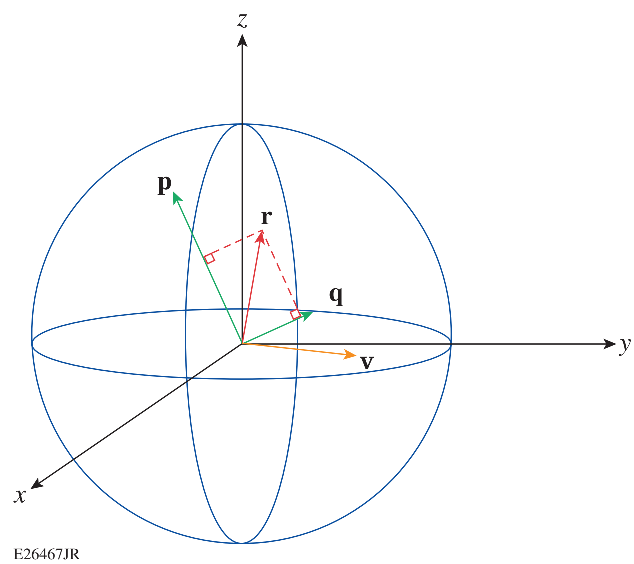

Figure 151.26
Vector representation displaying view direction, solution direction, and unit vectors of image plane with respect to each other.

$$\mathbf{r}\cdot\mathbf{q}_1=r_x q_{x_1}+r_y q_{y_1}+r_z q_{z_1}, \tag{3}$$

$$\mathbf{r}\cdot\mathbf{p}_1=r_x p_{x_1}+r_y p_{y_1}+r_z p_{z_1}, \tag{4}$$

$$\mathbf{r}\cdot\mathbf{q}_2=r_x q_{x_2}+r_y q_{y_2}+r_z q_{z_2}, \tag{5}$$

$$\mathbf{r}\cdot\mathbf{p}_2=r_x p_{x_2}+r_y p_{y_2}+r_z p_{z_2}, \tag{6}$$

where 1 and 2 refer to the first and second view, respectively. The results can be combined into two different matrices by choosing to solve for $\mathbf{r}$ using either Eqs. (3), (4), and (5) or Eqs. (3), (4), and (6). This is equivalent to using the vertical offset from either camera 1 or 2. These choices can be written in matrix form as follows:

$$\overleftrightarrow{M}_{q_1 q_2 p_1} \cdot \mathbf{r} = \begin{bmatrix} r_{q_1} \\ r_{q_2} \\ r_{p_1} \end{bmatrix} = \begin{bmatrix} q_{x_1} & q_{y_1} & q_{z_1} \\ q_{x_2} & q_{y_2} & q_{z_2} \\ p_{x_1} & p_{y_1} & p_{z_1} \end{bmatrix} \begin{bmatrix} r_x \\ r_y \\ r_z \end{bmatrix}, \tag{7}$$

$$\overleftrightarrow{M}_{q_1 q_2 p_2} \cdot \mathbf{r} = \begin{bmatrix} r_{q_1} \\ r_{q_2} \\ r_{p_2} \end{bmatrix} = \begin{bmatrix} q_{x_1} & q_{y_1} & q_{z_1} \\ q_{x_2} & q_{y_2} & q_{z_2} \\ p_{x_2} & p_{y_2} & p_{z_2} \end{bmatrix} \begin{bmatrix} r_x \\ r_y \\ r_z \end{bmatrix}. \tag{8}$$

Inverting the matrices gives two possible solutions to the offset as follows:

$$\mathbf{r}_{121} = \overleftrightarrow{M}^{-1}_{q_1 q_2 p_1} \cdot \mathbf{r}_{q_1 q_2 p_1}, \tag{9}$$

$$\mathbf{r}_{122} = \overleftrightarrow{M}^{-1}_{q_1 q_2 p_2} \cdot \mathbf{r}_{q_1 q_2 p_2}. \tag{10}$$

The average of these two solutions is the choice used in this method and is given by

$$\mathbf{r} = \frac{\left(\mathbf{r}_{121} + \mathbf{r}_{122}\right)}{2}. \tag{11}$$

To improve the accuracy of determining **r**, values are computed from as many quasi-orthogonal camera pairs as possible. The results are averaged and the standard deviations of the values are used as an estimate of the errors of these values.

The second method of determining **r** uses a least-squares approach. For a given assumed offset of the target **r**, the values r_{q_i} and r_{p_i} that would be observed in the ith view are given by

$$r_{q_i} = r_x q_x + r_y q_y + r_z q_z, \tag{12}$$

$$r_{p_i} = r_x p_x + r_y p_y + r_z p_z. \tag{13}$$

The least-squares search is performed to minimize the quantity χ^2 given by

$$\chi^2 = \sum_i \left(\Delta r_{\perp,i}\right)^2 w_i^2, \tag{14}$$

where the values w_i are the weights given to the ith view and the quantities $\Delta r_{\perp,i}$ are the perpendicular offsets in the ith view in turn given by

$$\Delta r_{\perp,i} = \sqrt{\left(r_{q_i} - \Delta q_i\right)^2 + \left(r_{p_i} - \Delta p_i\right)^2}, \tag{15}$$

where Δq_i and Δp_i are the horizontal and vertical offsets of the target in the ith view. The value of **r** that minimizes χ^2 is taken as the best value, while the error dr is given by

$$\mathrm{d}r = \left(\chi^2 \Big/ \sum w_i\right)^{1/2} \tag{16}$$

and is equivalent to the error of the mean of the best-fit value. When only two views are available, the first method of determining **r** is the best method to use, whereas when more than two views are available, the second method gives the most unbiased result. Table 151.I shows the current set of fixed XRPC's used in this position analysis. Typical errors when determining the position are ~3 to 5 μm.

Table 151.I: X-ray pinhole camera (XRPC) parameters.

Camera	Position θ (°)	Position ϕ (°)	Magnification
h4	29.52* 45.23**	234.00	4.047* 3.861**
h8	79.30	153.78	2.028
h12	108.89	54.00	4.000
h13	9.74	342.00	4.043
p2	68.43	54.00	3.992

*Before 17 March 2017
**After 17 March 2017

Measurement of Implosion Core Offsets

The implosion cores are imaged by the gated monochromatic x-ray imager (GMXI)[12] operating in time-integrating mode with four CID cameras recording the four images formed by the Kirkpatrick–Baez (KB) microscope optical assembly. Two of these images (GMXI-c and GMXI-d, filtered by 50.8 and 76.2 μm of Al, respectively) had signal levels that did not exceed the capacity of the CID cameras for all cryogenic and non-cryogenic target experiments that determined reference core positions. As for determining the t_0 offset, the non-cryogenic reference target is assumed to be perfectly centered at TCC. The energy bands are approximately the same for these two images being ~5 to 8 keV and ~5.5 to 8 keV for images GMXI-c and GMXI-d, respectively. The GMXI cameras observe the implosion cores from the common spherical coordinates θ = 96.02°, ϕ = 54° with respect to the target plane (each being ~1° away).

In contrast to the t_0 images where the limb of the image is used to determine the center, core images are centrally peaked, so the centroid is a better measure of the core's position in the CID image. Figure 151.27 shows example GMXI images, trimmed to 200 × 200 μm. The reference images used in this case are from a target experiment with a non-cryogenic target consisting of an 18-μm-thick CH shell filled with 3 atm of D_2 gas, imploded with the same pulse shape used on the subsequent cryogenic target shots [these are referred to as pulse-shape setup (PSS) shots]. Figures 151.27(a) and 151.27(b) are from the reference non-cryogenic target implosion (OMEGA shot 81056, GMXI-c and GMXI-d images); Figs. 151.27(c) and 151.27(d) are from a cryogenic target implosion (OMEGA shot 81060,

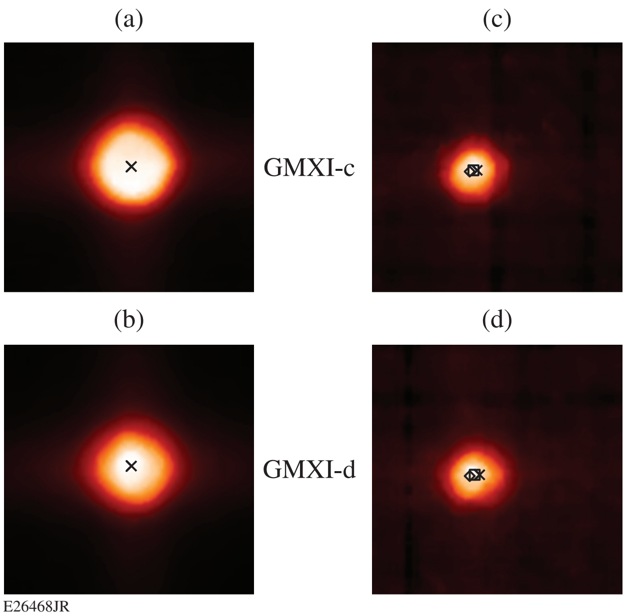

Figure 151.27
Four 200 × 200-μm gated monochromatic x-ray imager (GMXI) images, including a reference and a cryogenic shot. The "×" represents the centroid centers, diamonds represent the cross-correlation maximums, and squares represent the averages between those points. The offset of OMEGA shot 81060 from OMEGA shot 81056 is (–22.0,–5.0)±(0.0,2.0).

GMXI-c and GMXI-d images). The "×" symbols denote the centroids of the images; the diamond symbols on the GMXI-c and GMXI-d images of OMEGA shot 81060 show the points of maximum cross correlation between the cryogenic and PSS shots in the GMXI-c and GMXI-d images, respectively. The square symbols on shot 81060 images denote the averages between the centroid centers and the cross-correlation maximums. The amount of core offset is taken as the amount by which the image must be shifted to maximize the cross correlation. Figure151.28 shows the core offsets determined from the GMXI-c and GMXI-d images for a large number of cryogenic target shots; their consistency is evident. The average offset of the GMXI-c and GMXI-d images is therefore taken as the offset and the difference is an estimate of the error of this offset.

The t_0 offsets are compared with the GMXI offsets by computing the projections of the t_0 offsets in the view of the GMXI in the horizontal and vertical directions $q_{0,\mathrm{GMXI}}$ and $p_{0,\mathrm{GMXI}}$, respectively, given by

$$q_{0,\mathrm{GMXI}} = \mathbf{r} \cdot \mathbf{q}_{\mathrm{GMXI}}, \tag{17}$$

$$p_{0,\mathrm{GMXI}} = \mathbf{r} \cdot \mathbf{p}_{\mathrm{GMXI}}, \tag{18}$$

where $\mathbf{q}_{\mathrm{GMXI}}$ and $\mathbf{p}_{\mathrm{GMXI}}$ are the horizontal and vertical vectors, respectively, of the GMXI view. Since there is no other digitally recorded view of the core, the three-space core offset cannot be determined but the GMXI core offset and the projection of the t_0 offset into the GMXI view can be compared.

Results

Figures 151.29 and 151.30 show the measured core offsets compared to the projected t_0 offsets for horizontal, vertical, and

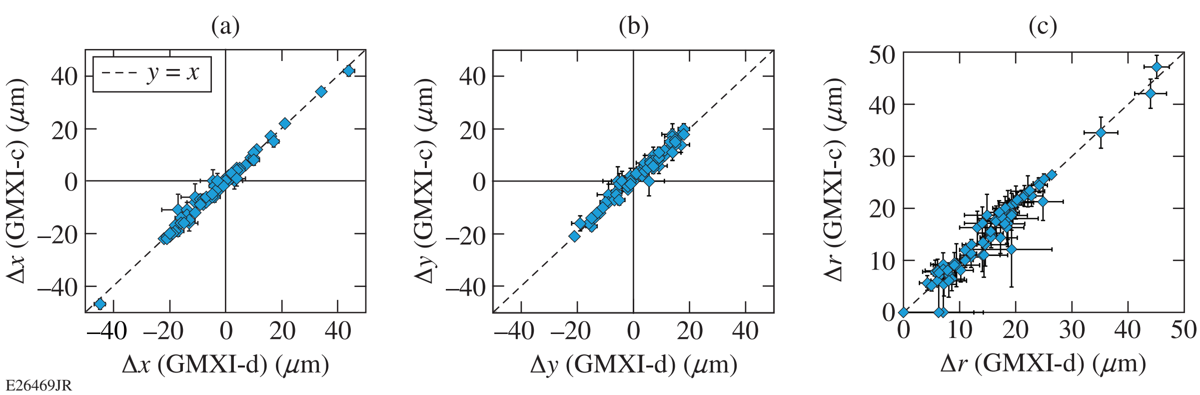

Figure 151.28
Comparisons of implosion core offset coordinates, GMXI-c against GMXI-d. Errors were calculated using the rms deviations from the lines of best fit, which are very nearly $y = x$ lines.

radial directions, respectively. The offsets in Fig. 151.29 are for a quasi-uniformly distributed sample of cryogenic target shots that span offsets from near zero to >100 μm and whose offset directions were nearly perpendicular to the GMXI view direction. Figure 151.29(a) shows that the horizontal displacement of the core is in the same direction as the t_0 offset and nearly equal in magnitude; i.e., the core is forming at approximately the position of the offset target center. In large part the core offsets confirm the accuracy of the t_0 offsets. Figure 151.30 compares the horizontal, vertical, and radial offsets of the implosion cores and the projected t_0 offsets for all recent cryogenic target shots (since 2015). The horizontal components of the t_0 and core offsets [Fig. 151.30(a)] are approximately uniformly distributed about the origin and most are <20 μm. The few large horizontal offsets agree in direction and are nearly of the same magnitude. In contrast, the vertical t_0 offsets are biased toward positive offset (in this case, from the TCC reference), whereas the core vertical offsets (y axis) are more uniformly distributed between positive and negative values. The reason for the positive bias of the t_0 vertical target offset is not known, but it is suggestive that the cryogenic targets are systematically above TCC at t_0 with an average offset of ~5 μm.

A large offset is expected to have a very detrimental effect on the fusion neutron yield, and even small offsets are calculated to have an effect on the yield under ideal simulated conditions,[13] so placing the target at TCC as accurately as possible is desired. But in real experimental conditions where many other factors may affect the implosion in addition to target offset, it may be difficult to assess the importance of target offset alone. To explore this dependence, the measured neutron yield divided by the calculated yield [yield-over-clean (YOC)] by the 1-D hydrocode *LILAC*[6] is plotted in Fig. 151.31 as a function of the measured t_0 offset for all recent cryogenic target shots (since 2015). Figure 151.31 shows that the YOC varies from ~0.2 to 0.7 for offsets less than ~15 μm and is smaller (~0.3 or less)

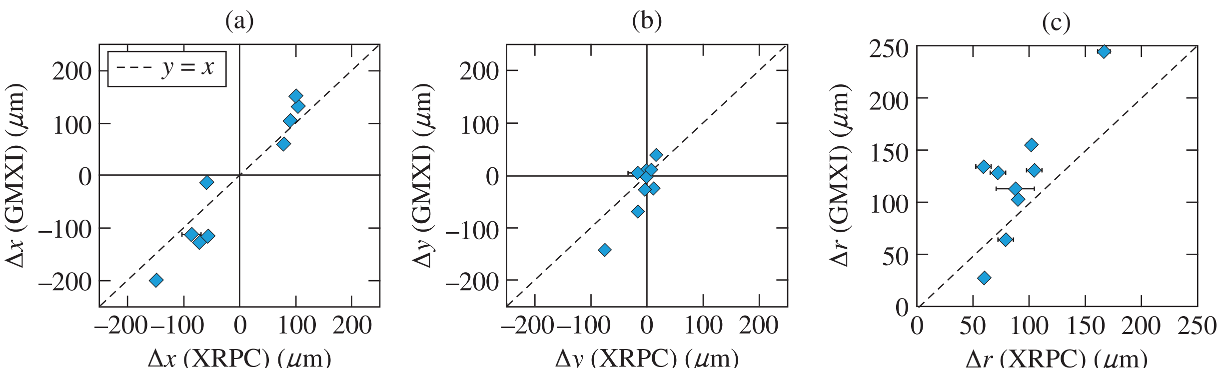

E26470JR

Figure 151.29
Comparisons of earlier OMEGA shots with large offset, implosion core positions against t_0 positions.

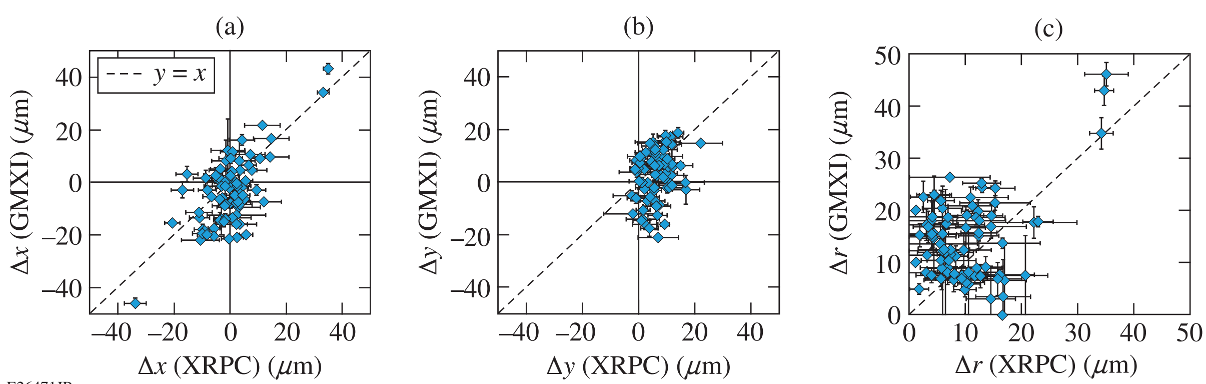

E26471JR

Figure 151.30
Comparisons of offset coordinates of implosion cores at image capture against the cores at time t_0.

for offsets greater than ~20 μm. These results are consistent with requiring a small offset to get a large value of the YOC but that a smaller value may be obtained at a small initial target offset for other unrelated reasons.

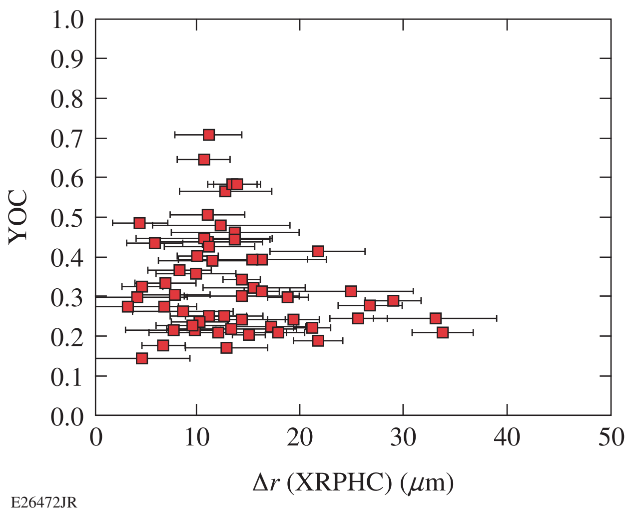

Figure 151.31
The measured cryogenic target neutron yield divided by the calculated yield ratio [yield-over-clean (YOC)] plotted as a function of the offset of the target at t_0.

Conclusions

This work describes the method for determining the offsets of cryogenic targets relative to the aim point of the OMEGA laser beams (t_0 offset) and shows measurements of the implosion core offsets from well-centered targets as determined in one direction (that of the GMXI). The t_0 offsets projected in the direction of the GMXI agree in direction and are close in magnitude to that of the core offsets with considerable scatter at small t_0 offsets (<20 μm). The approximate dependence of the YOC on target offset is such that no large YOC's are obtained when the t_0 offset is large (>20 μm). Knowing the accurate value of the t_0 offset is therefore critical in assessing the fusion performance of the implosion.

ACKNOWLEDGMENT

The authors acknowledge with gratitude the staff of the Laboratory for Laser Energetics for their work on ICF using the OMEGA Laser System. This material is based upon work supported by the Department of Energy National Nuclear Security Administration under Award Number DE-NA0001944, the University of Rochester, and the New York State Energy Research and Development Authority. The support of the DOE does not constitute an endorsement by the DOE of the views expressed in this paper.

REFERENCES

1. J. D. Lindl *et al*., Phys. Plasmas **11**, 339 (2004).
2. S. Atzeni and J. Meyer-ter-Vehn, *The Physics of Inertial Fusion: Beam Plasma Interaction, Hydrodynamics, Hot Dense Matter*, International Series of Monographs on Physics (Clarendon Press, Oxford, 2004).
3. R. Betti, K. Anderson, V. N. Goncharov, R. L. McCrory, D. D. Meyerhofer, S. Skupsky, and R. P. J. Town, Phys. Plasmas **9**, 2277 (2002).
4. E. M. Campbell and W. J. Hogan, Plasma Phys. Control. Fusion **41**, B39 (1999).
5. V. N. Goncharov, T. C. Sangster, R. Betti, T. R. Boehly, M. J. Bonino, T. J. B. Collins, R. S. Craxton, J. A. Delettrez, D. H. Edgell, R. Epstein, R. K. Follet, C. J. Forrest, D. H. Froula, V. Yu. Glebov, D. R. Harding, R. J. Henchen, S. X. Hu, I. V. Igumenshchev, R. Janezic, J. H. Kelly, T. J. Kessler, T. Z. Kosc, S. J. Loucks, J. A. Marozas, F. J. Marshall, A. V. Maximov, R. L. McCrory, P. W. McKenty, D. D. Meyerhofer, D. T. Michel, J. F. Myatt, R. Nora, P. B. Radha, S. P. Regan, W. Seka, W. T. Shmayda, R. W. Short, A. Shvydky, S. Skupsky, C. Stoeckl, B. Yaakobi, J. A. Frenje, M. Gatu-Johnson, R. D. Petrasso, and D. T. Casey, Phys. Plasmas **21**, 056315 (2014).
6. J. Delettrez, R. Epstein, M. C. Richardson, P. A. Jaanimagi, and B. L. Henke, Phys. Rev. A **36**, 3926 (1987).
7. I. V. Igumenshchev, V. N. Goncharov, F. J. Marshall, J. P. Knauer, E. M. Campbell, C. J. Forrest, D. H. Froula, V. Yu. Glebov, R. L. McCrory, S. P. Regan, T. C. Sangster, S. Skupsky, and C. Stoeckl, Phys. Plasmas **23**, 052702 (2016).
8. R. A. Forties and F. J. Marshall, Rev. Sci. Instrum. **76**, 073505 (2005).
9. F. J. Marshall, T. Ohki, D. McInnis, Z. Ninkov, and J. Carbone, Rev. Sci. Instrum. **72**, 713 (2001).
10. R. N. Bracewell, *Two-Dimensional Imaging* (Prentice Hall, Englewood Cliffs, NJ, 1995), pp. 286–288.
11. F. J. Marshall, T. DeHaas, and V. Yu. Glebov, Rev. Sci. Instrum. **81**, 10E503 (2010).
12. F. J. Marshall and J. A. Oertel, Rev. Sci. Instrum. **68**, 735 (1997).
13. S. X. Hu, P. B. Radha, J. A. Marozas, R. Betti, T. J. B. Collins, R. S. Craxton, J. A. Delettrez, D. H. Edgell, R. Epstein, V. N. Goncharov, I. V. Igumenshchev, F. J. Marshall, R. L. McCrory, D. D. Meyerhofer, S. P. Regan, T. C. Sangster, S. Skupsky, V. A. Smalyuk, Y. Elbaz, and D. Shvarts, Phys. Plasmas **16**, 112706 (2009).